GEOPHYSICS, VOL. 82, NO. 3 (MAY-JUNE 2017); P. S197–S205, 16 FIGS.
10.1190/GEO2016-0253.1

Imaging near-surface heterogeneities by natural migration of backscattered surface waves: Field data test

Zhaolun Liu[1], Abdullah AlTheyab[2], Sherif M. Hanafy[1], and Gerard Schuster[1]

ABSTRACT

We have developed a methodology for detecting the presence of near-surface heterogeneities by naturally migrating backscattered surface waves in controlled-source data. The near-surface heterogeneities must be located within a depth of approximately one-third the dominant wavelength λ of the strong surface-wave arrivals. This natural migration method does not require knowledge of the near-surface phase-velocity distribution because it uses the recorded data to approximate the Green's functions for migration. Prior to migration, the backscattered data are separated from the original records, and the band-passed filtered data are migrated to give an estimate of the migration image at a depth of approximately one-third λ. Each band-passed data set gives a migration image at a different depth. Results with synthetic data and field data recorded over known faults validate the effectiveness of this method. Migrating the surface waves in recorded 2D and 3D data sets accurately reveals the locations of known faults. The limitation of this method is that it requires a dense array of receivers with a geophone interval less than approximately one-half λ.

INTRODUCTION

The scattered surface wave generated by strong heterogeneities in the shallow subsurface is often seen as noise in seismic reflection records (Blonk et al., 1995; Ernst et al., 2002); however, this noise can also be used as signal if the backscattered data are migrated to image the near-surface heterogeneities (Snieder, 1986; Riyanti, 2005; Yu et al., 2014; Almuhaidib and Toksöz, 2015; Hyslop and Stewart, 2015).

The conventional surface-wave imaging methods are based on the Born approximation of surface waves, which require an estimation of the background velocity model and the weak scattering approximation. Under the Born approximation, the backscattered surface wave data $\mathbf{d}$ are denoted as $\mathbf{d} = \mathbf{Lm}$, where $\mathbf{L}$ is the forward modeling operator for a known background velocity and $\mathbf{m}$ is the model perturbation (Snieder, 1986; Tanimoto, 1990). To invert for the model perturbation $\mathbf{m}$, Riyanti (2005) uses an iterative optimization method to calculate the solution. In contrast, Snieder (1986) and Yu et al. (2014) apply the adjoint of the forward modeling operator $\mathbf{L}^{\dagger}$ to the scattered data to obtain the migration image.

Apart from the methods based on the Born approximation, Hyslop and Stewart (2015) estimate the surface-wave reflection coefficients at near-surface lateral discontinuities by a processing flow based on a 2D semianalytic forward modeling method for surface-wave propagation. They then map the frequency-dependent reflection coefficients to depth to produce a 2D reflectivity map of discontinuities.

Recently, AlTheyab et al. (2015, 2016) introduced the natural migration (NM) method to image the near-surface heterogeneities, assuming that the scattering bodies are within a depth of approximately one-third wavelength from the free surface. It also requires a dense distribution of sources and receivers to avoid aliasing artifacts in the migration image. There are several benefits to the NM method. First, no Born approximation is used, so that strongly scattered events can be migrated to the surface projection of their origin. Second, no velocity model is needed because the Green's functions in the migration kernels are recorded as band-limited shot gathers, in which the sources and receivers are located on the surface.

AlTheyab et al. (2016) demonstrate the effectiveness of the NM method with ambient noise data, but they do not show it to be effective for controlled-source data. This paper now presents a general procedure for the NM method applied to controlled-source data, and it shows the results of applying NM to surface-wave data. Results show that NM of backscattered surface waves can detect

Manuscript received by the Editor 14 May 2016; revised manuscript received 30 November 2016; published online 27 February 2017.
[1]King Abdullah University of Science and Technology, Department of Earth Science and Engineering, Thuwal, Saudi Arabia. E-mail: zhaolun.liu@kaust.edu.sa; sherif.mahmoud@kaust.edu.sa; gerard.schuster@kaust.edu.sa.
[2]Formerly King Abdullah University of Science and Technology, Department of Earth Science and Engineering, Thuwal, Saudi Arabia; presently Saudi Aramco, Eastern Area Exploration Department, Dhahran, Saudi Arabia. E-mail: abdullah.altheyab@kaust.edu.sa.

near-surface heterogeneities, which can indicate the existence of faults or low-velocity zones (LVZs).

THEORY OF NATURAL MIGRATION

Assuming that the vertical component of the scattered Rayleigh wave $u(\mathbf{x}_s, \mathbf{x}_r)$ due to an impulsive point source in the vertical direction at $\mathbf{x}_s$ is recorded by the receiver at $\mathbf{x}_r$, the natural migration equation in the frequency domain can be expressed as (AlTheyab et al., 2016)

$$m(\mathbf{x}) = \sum_{s,r \in B} \int 2\omega^2 W(\omega)^* G(\mathbf{x}|\mathbf{x}_s)^* G(\mathbf{x}|\mathbf{x}_r)^* u(\mathbf{x}_s, \mathbf{x}_r) d\omega, \tag{1}$$

where $m(\mathbf{x})$ is the perturbation model that represents an arbitrary distribution of elastic-parameter perturbations at the image point $\mathbf{x}$ and $*$ denotes complex conjugation. Here, ω is the angular frequency, $W(\omega)$ represents the source-wavelet spectrum and is assumed to be $W(\omega) = A(\omega)e^{-iwt_0}$, which is a zero-phase wavelet with the time delay of t_0, and $A(\omega)$ is the amplitude spectrum; B is a set of source and receiver positions at the surface (just below the free surface); and $\mathbf{x}$, $\mathbf{x}_s$, and $\mathbf{x}_r$ are the migration image, source, and receiver positions in set B, respectively. Note that the possible positions of the trial image point $\mathbf{x}$ can only be where the sources or receivers are located near the surface. The function $G(\mathbf{x}|\mathbf{x}_s)$ is the Green's function for the vertical-component harmonic point source at $\mathbf{x}_s$ and receiver at $\mathbf{x}$, and $G(\mathbf{x}|\mathbf{x}_r)$ is the Green's function for a vertical-component-particle-velocity recording that only contains the transmitted wavefield without backscattering.

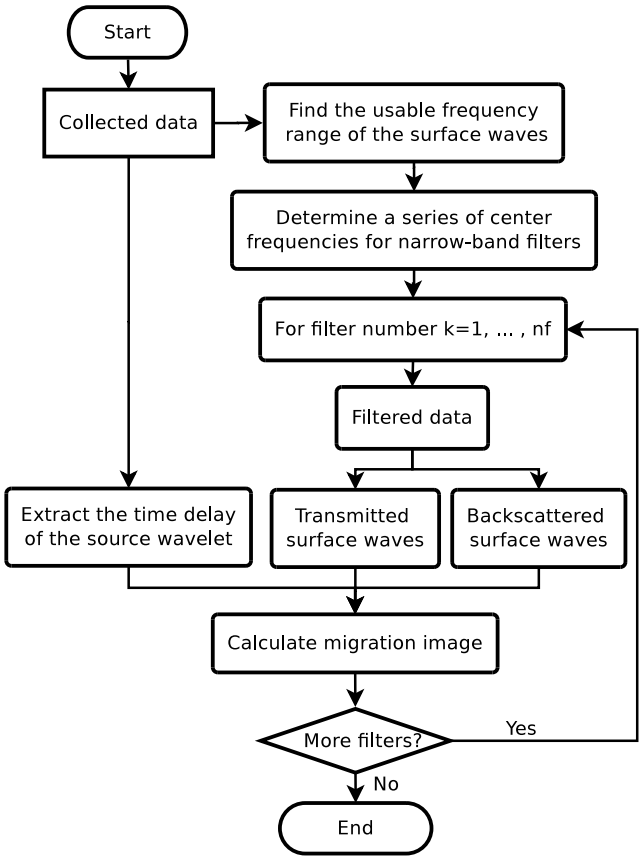

Figure 1. The natural migration workflow for active-source data.

The wavefield $u(\mathbf{x}|\mathbf{x}_s)$ is equal to $W(\omega)G(\mathbf{x}|\mathbf{x}_s)$, so that the Green's function can be expressed as

$$G(\mathbf{x}|\mathbf{x}_s) = u(\mathbf{x}|\mathbf{x}_s)W(\omega)^{-1}. \tag{2}$$

Substituting equation 2 into equation 1 gives the natural migration equation for active-source data

$$\begin{aligned} m(\mathbf{x}) &= \sum_{s,r} \int 2\omega^2 [W(\omega)^{-1} u(\mathbf{x}|\mathbf{x}_s) u(\mathbf{x}|\mathbf{x}_r)]^* u(\mathbf{x}_s, \mathbf{x}_r) d\omega, \\ &= \sum_{s,r} L(\mathbf{x}_r|\mathbf{x}|\mathbf{x}_s)^* u(\mathbf{x}_s, \mathbf{x}_r), \end{aligned} \tag{3}$$

where $L(\mathbf{x}_r|\mathbf{x}|\mathbf{x}_s) = \int d\omega 2\omega^2 W(\omega)^{-1} u(\mathbf{x}|\mathbf{x}_s) u(\mathbf{x}|\mathbf{x}_r)$ is the forward modeling operator. To calculate $L(\mathbf{x}_r|\mathbf{x}|\mathbf{x}_s)$, the deconvolution filter $W(\omega)^{-1}$ must be estimated. Ignoring the amplitude term $A(\omega)$ of $W(\omega)$, we only estimate the time delay t_0 from the near-offset transmitted surface-wave arrivals. The deconvolution filter $W(\omega)^{-1}$ is then approximated as e^{iwt_0}.

The migration image $m(\mathbf{x})$ for $\mathbf{x} \in B$ in equation 3 can be seen as the projection of the scatterer at shallow depths onto the surface denoted by the set of points B (Campman et al., 2005). Moreover, migration images at B can be mapped to different depths in the medium based on the principle that surface waves at lower frequencies are more sensitive to the presence of deeper scatterers. Therefore, u in equation 3 should be filtered by a narrowband filter prior to migration.

WORKFLOW OF NATURAL MIGRATION FOR CONTROLLED-SOURCE DATA

The workflow for migrating the back-scattered surface waves with equation 3 is shown in Figure 1, which is summarized in the following five steps. Additional details are given in AlTheyab et al. (2016).

1) Find the usable frequency range of the surface waves in the data.
2) Determine the center frequencies of overlapping narrowband filters for data filtering. The minimum center frequency is selected that provides an acceptable signal-to-noise ratio in the data. The maximum center frequency has to be smaller than $v_{\min}/(2\Delta x)$ to avoid horizontal spatial aliasing of the migration image, where $v_{\min}$ is the minimum phase velocity and Δx is the spatial spacing of the traces. However, as shown in the following synthetic results, the NM method can generate usable migration images of near-surface lateral heterogeneities with aliased data.
3) Extract the time delay t_0 of the source wavelet $W(\omega)$ in equation 3 from the near-offset transmitted surface-wave arrivals. The deconvolution filter $W(\omega)^{-1}$ in equation 3 is then approximated as e^{iwt_0}.
4) Separate the scattered surface waves from other arrivals, especially the transmitted surface waves. In our examples, the seismic arrivals that arrive earlier than the transmitted surface waves are muted. An alternative is to use FK filtering to estimate the backscattered surface waves. The muting window is computed from the estimated phase velocity of the recorded surface waves. The near-source wavefields are also muted to avoid the near-field strong artifacts.

5) Migrate the processed backscattered data to compute the migration image on the surface for different frequencies.

NUMERICAL RESULTS

Results are now shown for natural migration of surface waves for synthetic and field data. The field data are recorded for land surveys near the Gulf of Aqaba and the Qademah fault system in Saudi Arabia.

Natural migration of synthetic data

Synthetic shot gathers are computed by finite-difference solutions to the 3D elastic-wave equation (Virieux, 1986), with a free-surface boundary condition (Gottschämmer and Olsen, 2001). The source is a Ricker wavelet with a peak frequency of 20 Hz and a time delay of 0.05 s. The S-wave velocity model for modeling the data is shown in Figure 2, which has a buried fault at the depth of 6 m and an LVZ between 129 and 174 m. The P-wave velocity is calculated by $V_P = \sqrt{3}V_S$, and the density is constant with the value of 2.0 kg/m^3. The grid spacing of the model is 3 m in each direction. An areal acquisition array is distributed just below the free surface, and the source intervals are 10 and 20 m along the x- and y-directions, respectively. The receivers are at the same position as the sources, and the output data are vertical particle-velocity displacements. One of the common-shot gathers (CSGs) is shown in Figure 3a.

Seven narrowband filters with the peak frequencies ranging from 15 to 45 Hz are designed to image the subsurface heterogeneities at different depths. Because the receiver spacing is 10 m and the minimum-phase velocity is approximately 700 m/s (estimated from the dispersion curve), 35 Hz is the maximum frequency that

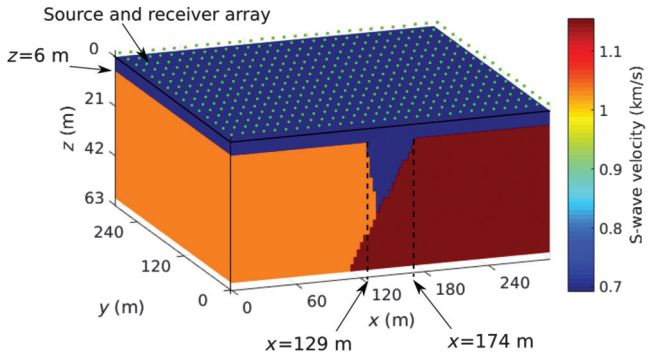

Figure 2. The 3D S-wave velocity model used for the synthetic tests with a 30 × 15 source and receiver array on the surface.

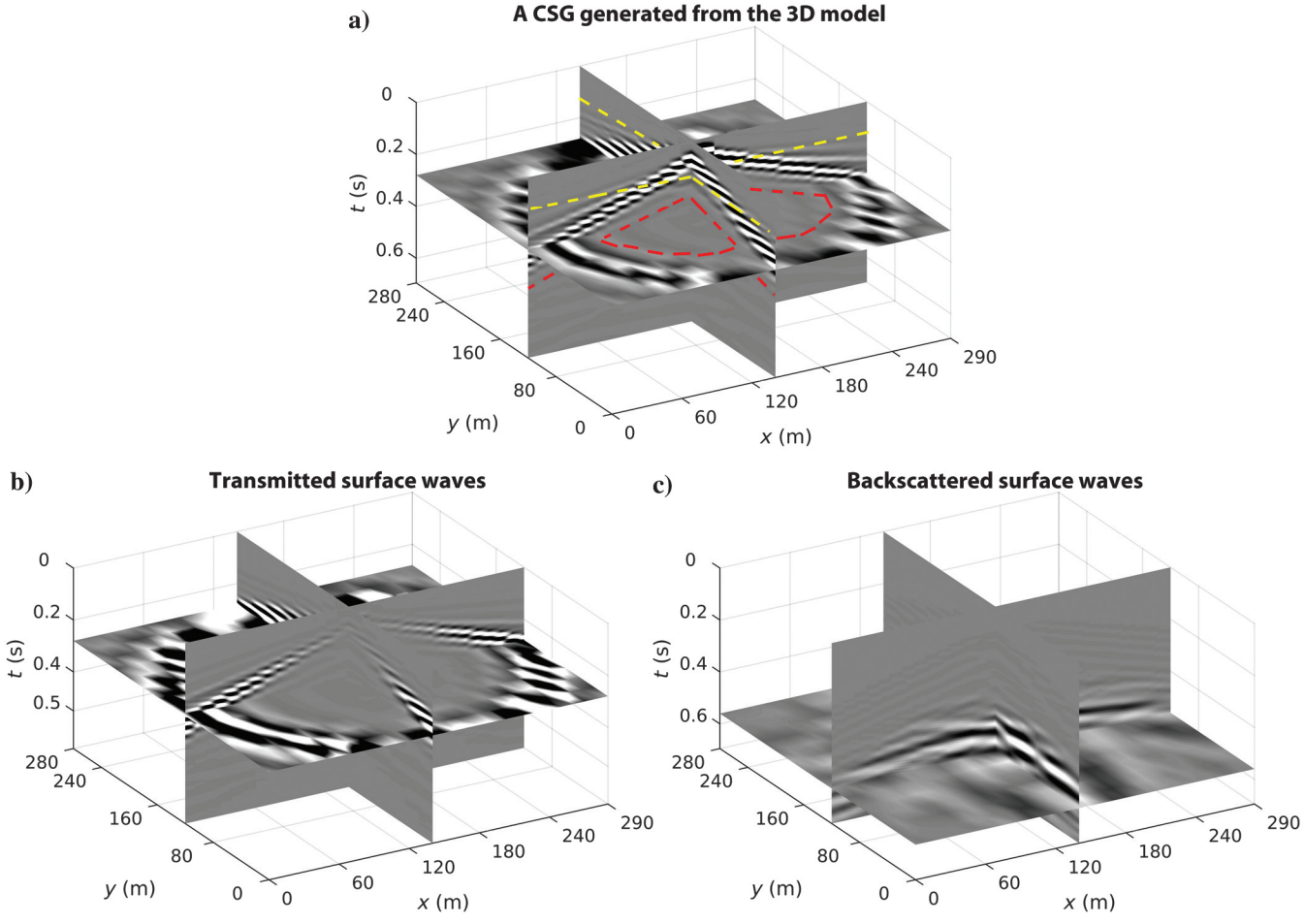

Figure 3. (a) A common-shot gather generated from the 3D model. The moveout velocity of the dashed red lines for the separation of transmitted and backscattered surface waves is approximately 500 m/s. The near-source arrivals are muted along the yellow lines (approximately 0.1 s). (b) Transmitted surface waves. (c) Backscattered surface waves.

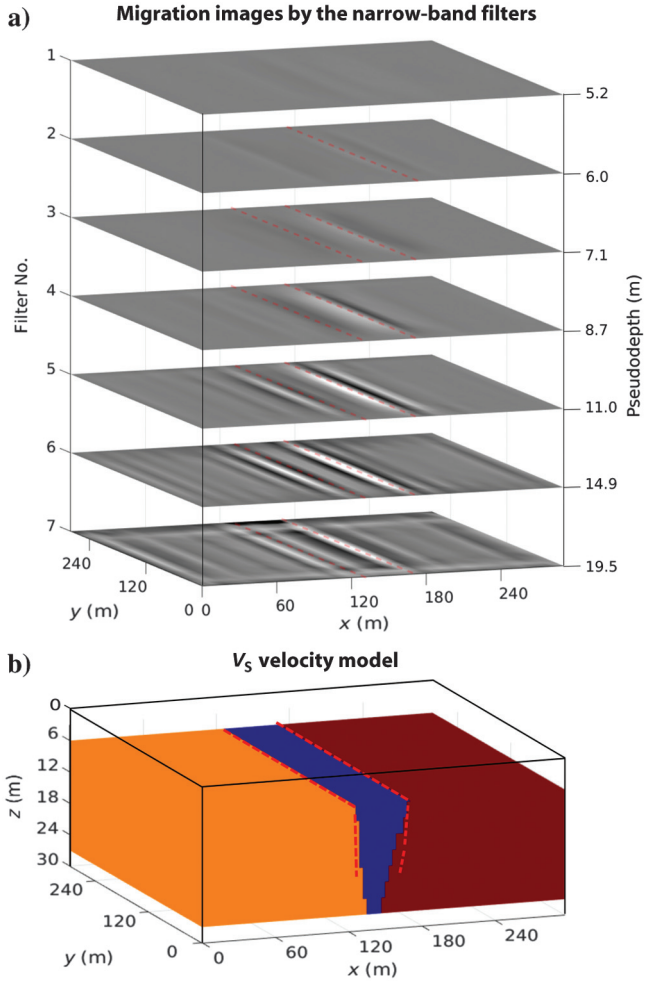

Figure 4. (a) The migration images at $z = 0$ m computed from the synthetic data with the narrowband filters from 1 to 7 (the center frequencies change from 45 to 15 Hz with a 5 Hz interval). The two dashed red lines are at $x = 129$ and 174 m, respectively, and the z-axis denotes the pseudodepth calculated from the mapping of frequency to the depth of one-third of a wavelength. (b) Upper portion of the V_S-velocity model and the dashed red lines are taken from (a).

avoids spatial aliasing. The band-pass filters with center frequencies greater than 35 Hz are used to assess the aliasing issues. The transmitted surface waves shown in Figure 3b are separated by the arrivals between the traveltimes indicated by the dashed yellow and red lines in Figure 3a. The backscattered surface waves shown in Figure 3c are separated by masking the arrivals earlier than the traveltimes of transmitted surface-wave arrivals, which are indicated by the dashed red lines in Figure 3a.

Each band-passed data set is used according to equation 3, and the migration images are shown in Figure 4a, where the two dashed red lines are at $x = 129$ and 174 m, respectively. Figure 4b shows the upper portion of the V_S-velocity model. The comparison

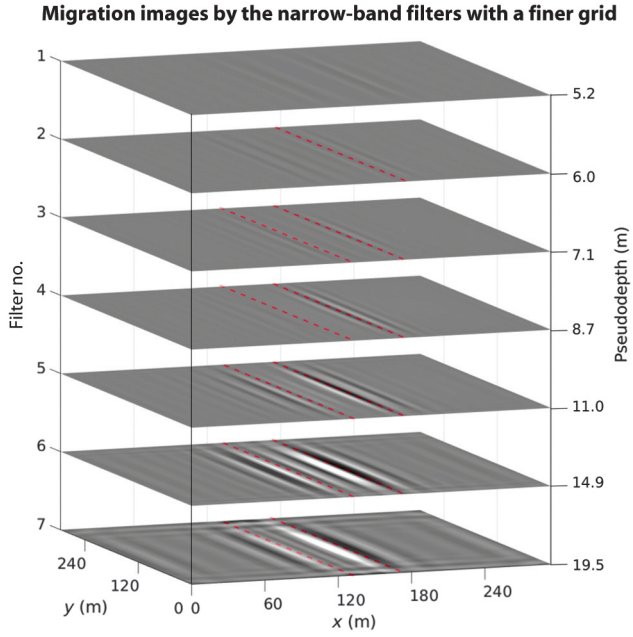

Figure 6. The migration images at $z = 0$ m computed from the synthetic data with a finer source and receiver spacing of 6 m, where the two dashed red lines are at $x = 129$ and 174 m, respectively, and the z-axis denotes the pseudodepth calculated from the mapping of frequency to the depth of one-third of a wavelength.

Figure 5. (a) The inline common-shot gather for the source at $x = 0$ m and $y = 0$ m, (b) its estimated phase-velocity dispersion curve, and (c) the curve that plots one-third of a wavelength against frequency.

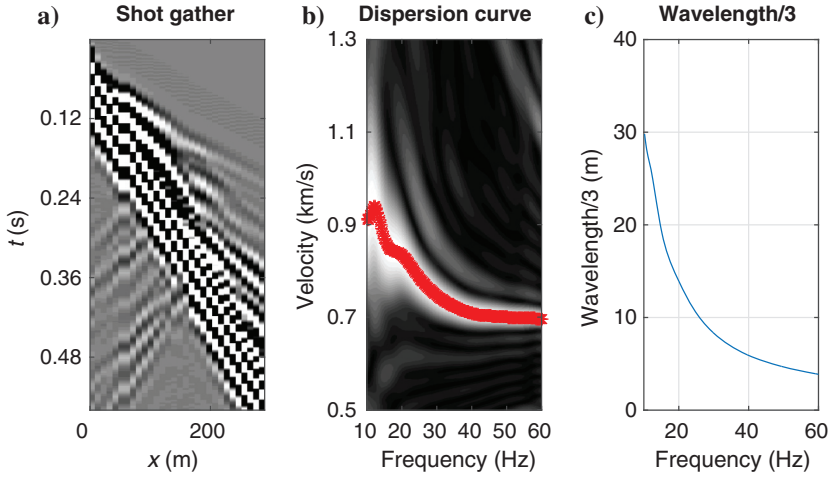

between the natural migration results by different filters shows that the migration images of the LVZ become more explicit as the peak frequency decreases. This is because the migration image from higher frequency data delineates the shallow part of the LVZ, whereas the deep part of the LVZ is imaged from the lower frequency data.

Surface waves are typically most sensitive to the velocity model to a depth of approximately one-third (some references choose one-half) of their wavelength (Stokoe and Nazarian, 1985; Hyslop and Stewart, 2015). Therefore, the depth range of each migration image can be estimated roughly by this relationship. We assign each peak frequency f_0 of the filtered data to the depth of approximately one-third the corresponding wavelength. We should note that this relationship is a rough approximation; however, similar mappings of direct surface-wave spectra to depth have been proven useful for near-surface interpretation (Shtivelman, 2000). The wavelength λ for each frequency can be approximated by $\lambda = c/f$, where c is the average phase velocity that can be obtained from the dispersion curves at selected source positions. An alternative procedure for relating the surface-wave frequency to the depth is by analyzing the sensitivity of the surface-wave phase velocity to the changes in the S-wave velocity at a specified depth (Xia et al., 1999).

Figure 5a and 5b shows an inline CSG for the source at $x = 0$ m and $y = 0$ m and its estimated phase-velocity dispersion curve. The curve that plots one-third wavelength against the frequency is shown in Figure 5c, where we can estimate the average wavelength for each frequency in the data. Figure 4a shows the pseudodepth for each migration image in the z-axis, where the dashed red lines in Figure 4a are mapped onto the V_S-velocity model shown in Figure 4b. The migration image provides a good estimate of the fault boundaries.

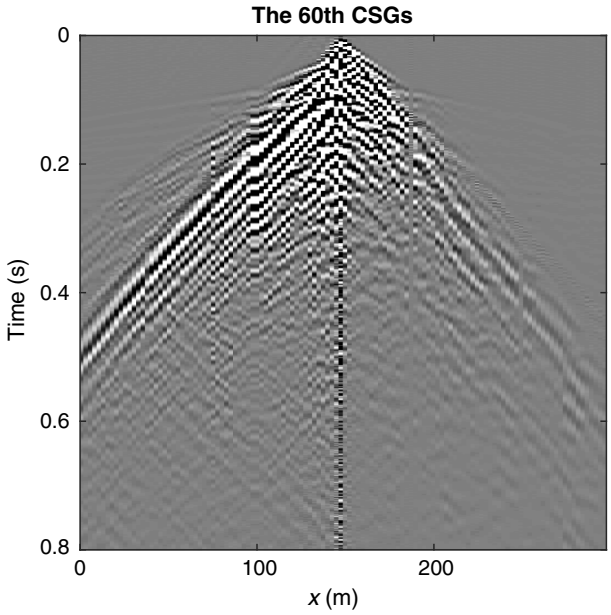

Figure 7. The 60th common-shot gather from the Aqaba data.

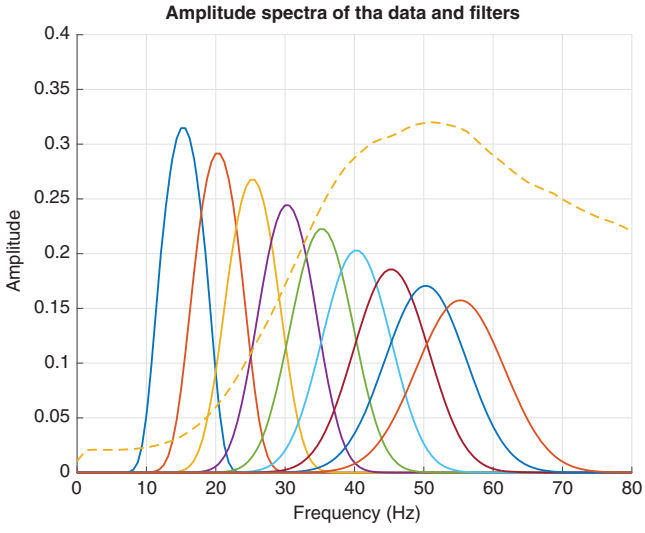

Figure 8. Solid lines denote the amplitude spectra of the nine band-pass filters; the dashed line denotes the amplitude spectrum of all 120 shot gathers in the Aqaba data.

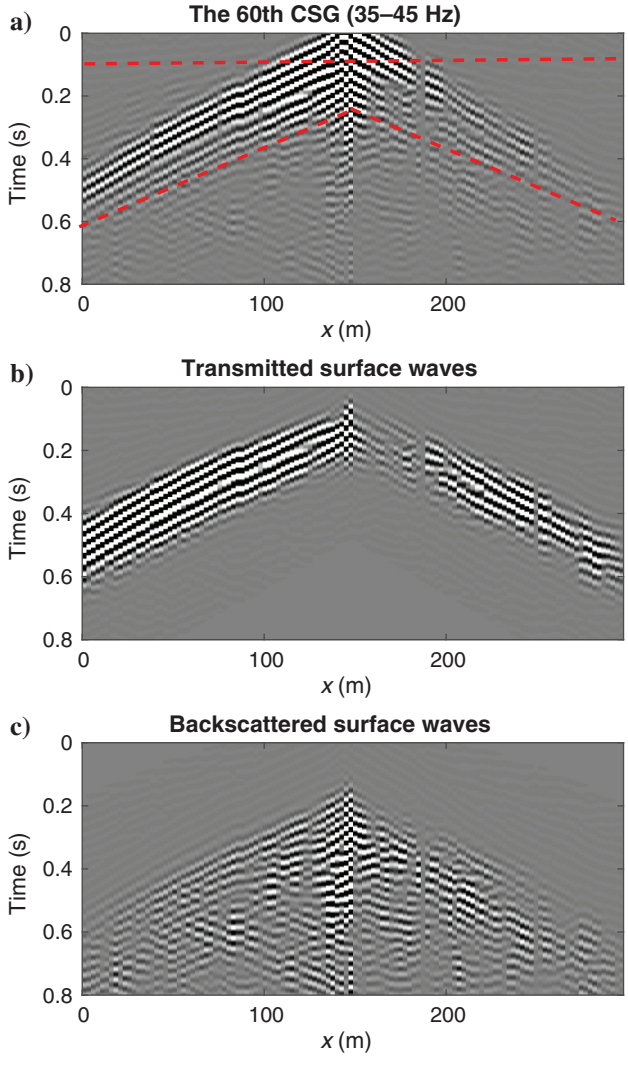

Figure 9. (a) The 60th common-shot gather filtered by the band-pass filter of 35–45 Hz; (b) the transmitted surface waves; and (c) the backscattered surface waves obtained by tapered muting of events above the inclined dashed lines.

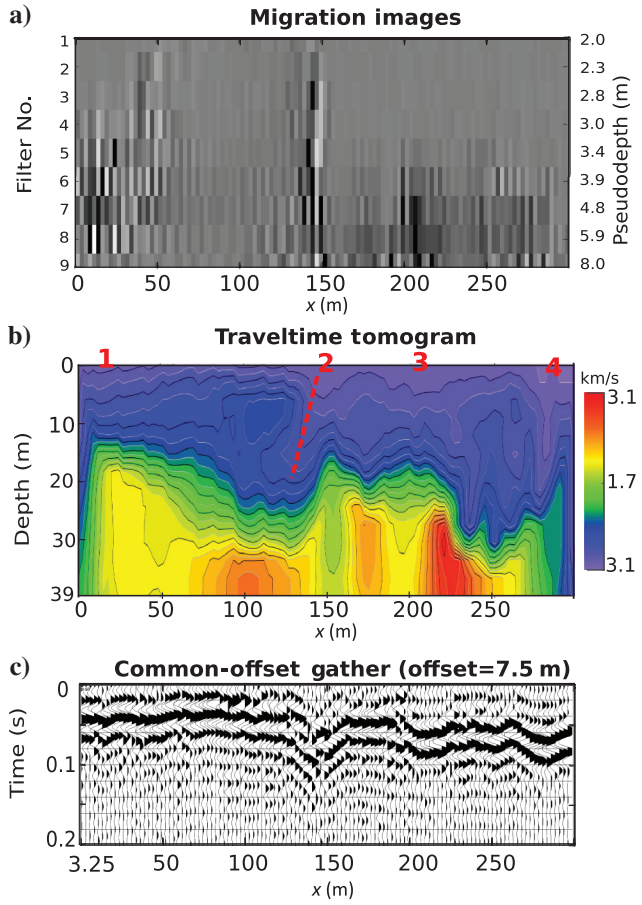

Figure 10. (a) Migration images for the Aqaba data with nine narrow-band filters, where the z-axis is the pseudodepth calculated from one-third of the wavelength, (b) traveltime tomogram, and (c) common-offset gather with 7.5 m offset. The locations denoted by 2–4 are clearly associated with horizontal velocity anomalies in all three illustrations; the horizontal velocity anomaly denoted by location 1 is also seen in the traveltime tomogram. A fault breaks the surface at location 2.

As a comparison, the migration images with a finer geophone spacing of 6 m are shown in Figure 6, where the maximum frequency that avoids spatial aliasing is approximately 58 Hz. Comparison of Figures 4a and 6 shows that the spatial aliasing artifacts are more prominent in the coarsely gridded model with center frequencies from 45 to 25 Hz. However, the migration images with spatial aliasing still show a blurred boundary at the lateral velocity contrast. A combination of images from different frequencies is helpful for interpreting the geologic events.

Natural migration of Aqaba data

A 2D land survey was carried out along the Gulf of Aqaba coast in Saudi Arabia (Hanafy et al., 2014). There were 120 shot gathers

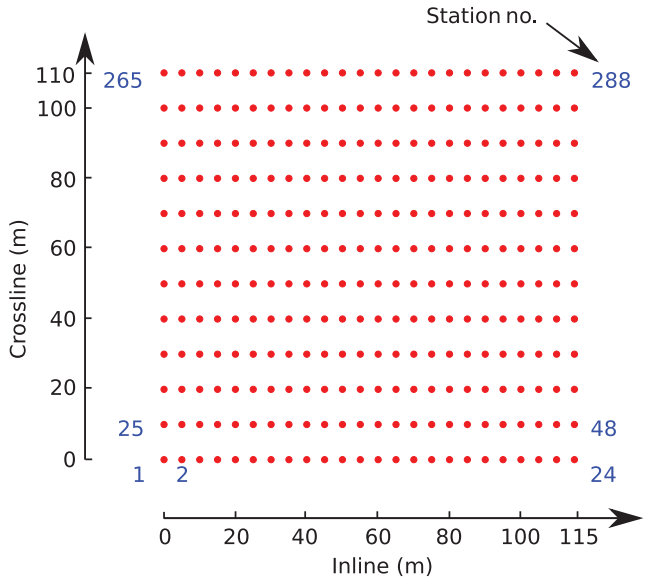

Figure 12. Receiver geometry for the Qademah fault data. Shots are located at each geophone, and a total of 288 shot gathers are migrated using equation 3.

Figure 11. (a) The first common-shot gather of the Aqaba data, (b) the phase-velocity dispersion curve, and (c) the curve that plots one-third of a wavelength against the frequency.

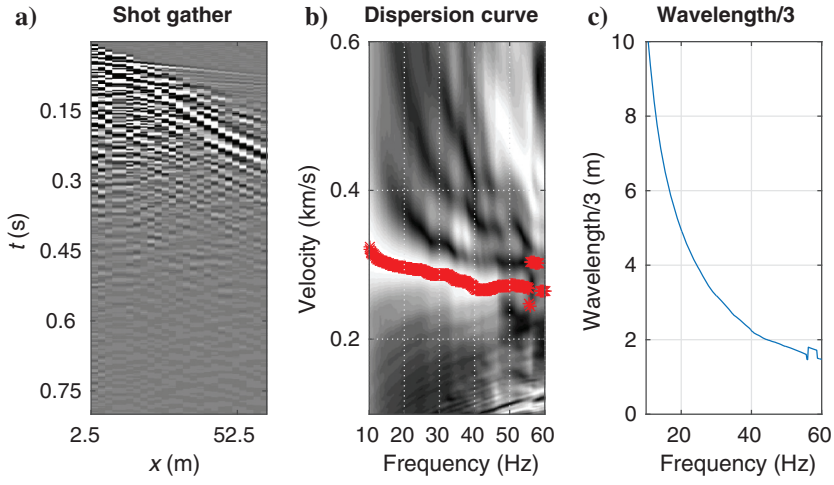

recorded, with shot and receiver intervals of 2.5 m. The source is generated by a 200-lb weight drop striking a metal plate on the ground, with 10–15 stacks at each shot location. A shot gather is shown in Figure 7, and the dashed line in Figure 8 shows the amplitude spectrum of all traces in the CSG.

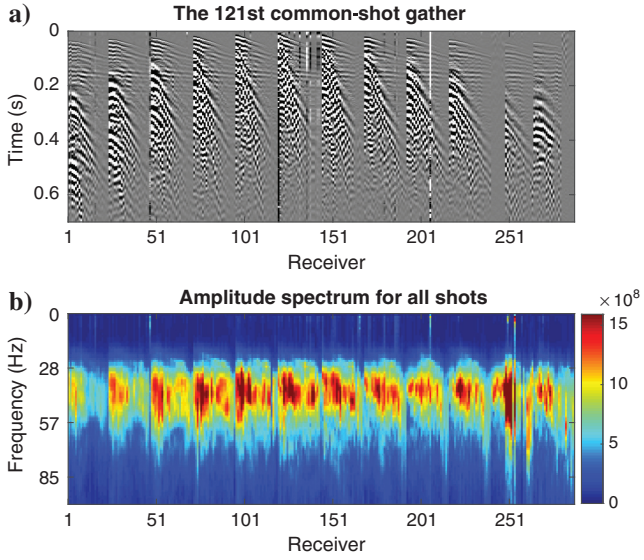

Figure 13. (a) The common-shot gather no. 121 from the Qademah fault data and (b) the amplitude spectrum for all 288 shot gathers.

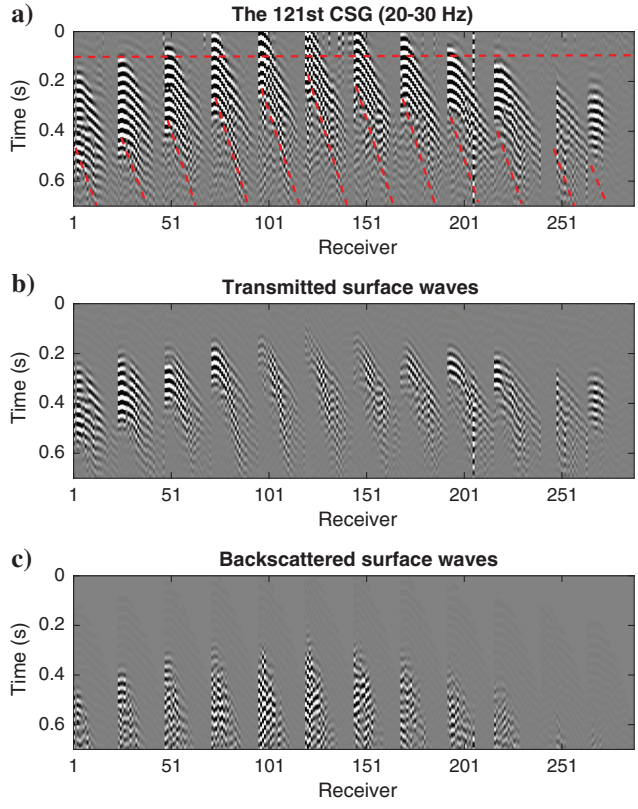

Figure 14. (a) Common-shot gather no. 121 from the Qademah fault data filtered by a 20–30 Hz band-pass filter and (b) the separated transmitted waves (a) along the red dip lines (slope = 140 m/s). (c) The separated backscattered waves along the horizontal red line (approximately 0.1 s).

A series of low-pass filters is used to find the maximum usable frequency of the surface waves in the data. Results show that the maximum frequency of the surface waves is approximately 45 Hz. Next, we design nine narrowband filters, and their center frequencies vary from 15 to 55 Hz with a 5-Hz interval. The amplitude spectra are shown in Figure 8, and Figure 9 shows the 60th CSG filtered between 35 and 45 Hz. The time delay of the source wavelet is estimated to be 0.05 s, and the transmitted and backscattered surface waves are separated along the traveltimes indicated by the inclined dashed line in Figure 9. The traveltimes are calculated based on the average phase velocity of 300 m/s.

Migrating the surface waves after applying nine narrowband filters to the shot gathers gives the migration images at $z = 0$ in Figure 10a. For these images, the main fault is located at $x = 150$ m on the surface, which is also observed in the field as the surface expression of a fault (Hanafy et al., 2014).

There are two other lateral velocity anomalies at $x = 205$ and 280 m (locations 3 and 4 in Figure 10b) in Figure 10a that are detected in the lower frequency migration images, which means that they are deeply buried. This is consistent with the traveltime

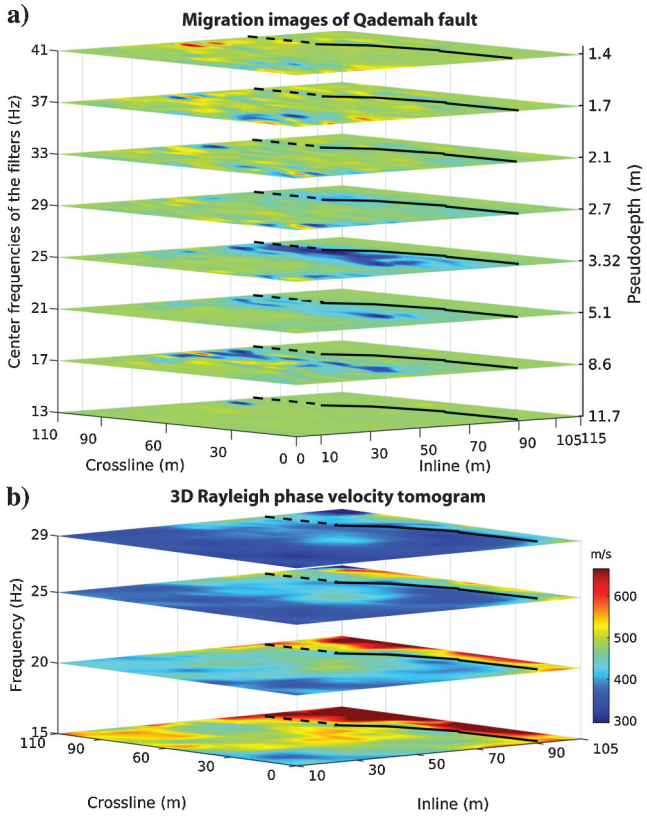

Figure 15. (a) Migration images computed from the Qademah fault data filtered by eight narrowband filters, where the center frequencies range from 41 (filter 1) to 13 Hz (filter 8). (b) The 3D Rayleigh phase-velocity tomogram (Hanafy, 2015). The location of the Qademah fault indicated by the black lines in the migration images shown in (a) correlate with the S-velocity tomogram shown in (b). There is no visible indication of the fault on the free surface. The dip angle of the fault interpreted from this migration image is similar to that estimated from the tomogram.

tomogram shown in Figure 10b, which suggests that there are faults or LVZs at these locations. The LVZs are clearly seen in the common-offset gathers at $x = 200$ and 280 m in Figure 10c, where abrupt changes in velocity are accompanied by sharp changes in the arrival times of the surface waves. In fact, a fault that breaks the surface is observed at the location 2. There also exists velocity anomalies between 0 and 50 m, which can be seen in the traveltime tomogram.

Figure 11b shows the dispersion curve of one CSG in Figure 11a. We notice that there is a discontinuity in the dispersion curve greater than 55 Hz, where the fundamental mode is weak. Figure 11c shows the wavelength plotted against frequency, which is calculated from the dispersion curve of the first common-shot gather. By averaging over several source positions, we can estimate the average wavelength for each frequency in the data set. And then, the pseudodepth for each migration image is estimated in Figure 10a.

This example illustrates that the surface-wave migration image can be interpreted at the locations of abrupt velocity changes in the tomogram, which can represent the existence of either a LVZ or a near-surface fault.

Natural migration of Qademah data

A 3D land survey was carried out along the Red Sea coast over the Qademah fault system, approximately 30 km north of the KAUST campus (Hanafy, 2015). There were 288 receivers arranged in 12 parallel lines, and each line has 24 receivers. The inline receiver interval is 5 m, and the crossline interval is 10 m, which is similar to that of the 3D survey geometry in Figure 2. The receiver geometry is shown in Figure 12, where one shot is fired at each receiver location for a total of 288 shot gathers. The source is generated by a 200-lb hammer striking a metal plate on the ground, and a shot gather is shown in Figure 13a. Figure 13b shows the composite amplitude spectrum of all the common-shot gathers over the frequency range between 15 and 55 Hz.

We designed eight narrowband filters with center frequencies ranging from 13 to 41 Hz to get the depth information of the migration image. The CSGs are band-pass filtered with a center frequency of 25 Hz, and CSG no. 121 is shown in Figure 14a, where the time shift of the source wavelet is approximately 0.1 s. The separated transmitted and backscattered surface waves for the 121st common-shot gather are shown in Figure 14b and 14c.

Applying equation 3 to 288 processed (see workflow in Figure 1) shot gathers gives the migration images in Figure 15a. The blue areas in Figure 15a show the images of near-surface heterogeneities associated with filters from 4 to 7, and the positions of these images vary from 45 to 85 m with increasing frequency in the data, which mostly agrees with the actual fault location indicated by traveltime tomography shown in Figure 15b (Hanafy, 2015). Figure 16a shows the first inline traces of the first CSG, and Figure 16b presents the estimated phase-velocity dispersion curve. Figure 16c plots the wavelength of surface waves for each frequency, based on the dispersion curve in Figure 16b. Averaging over several source positions, the average wavelength can be estimated for each frequency in the data. The pseudodepth for each migration image is shown in Figure 15a.

CONCLUSIONS

We present the natural migration method for controlled-source data, which can detect near-surface heterogeneities by naturally migrating the backscattered surface waves. The assumption is that the near-surface heterogeneities must be within a depth of approximately one-third the dominant wavelength of the surface waves. A dense receiver sampling (half the minimum wavelength of the surface waves) must be used to record the Green's functions at the surface to avoid spatial aliasing in the migration images. The NM method uses the recorded data along the surface to calculate Green's functions instead of computer stimulations that require the P- and S-velocity models. Synthetic and field results demonstrate that lateral near-surface heterogeneities can be imaged by NM of backscattered surface waves in common-shot gathers. No modeling of the 3D wave equation is needed. The implication is that more accurate hazard maps can be quickly generated by naturally migrating surface waves in land surveys in a cost-effective manner. The limitation of this method is that a dense receiver coverage is needed to get a high-resolution image. However, the NM method with aliased data can still provide migration images that delineate the locations of faults. Future research should explore the use of least-squares migration in mitigating these artifacts.

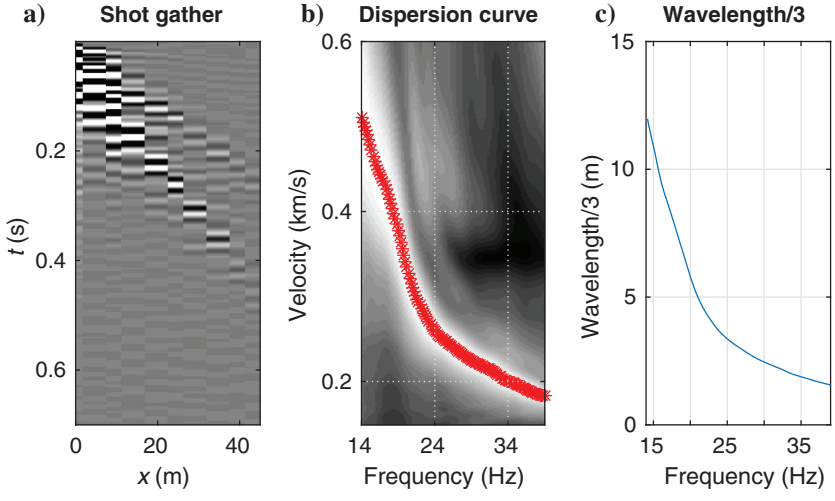

Figure 16. (a) The common-shot gather for traces along the x-direction for the first source shown in Figure 12, (b) estimated phase-velocity dispersion curve, and (c) one-third wavelength plotted against frequency.

ACKNOWLEDGMENTS

The research reported in this paper was supported by the King Abdullah University of Science and Technology (KAUST) in Thuwal, Saudi Arabia. We thank the sponsors of the Center for Subsurface Imaging and Fluid Modeling (CSIM) consortium for their support. We would also like to thank the high-performance computing center of KAUST for providing access to supercomputing facilities. We thank B. Guo and Z. Feng for editing the paper. A. AlTheyab thanks Saudi Aramco for sponsoring his graduate studies. We also thank the associate editor J. van der Neut and three anonymous reviewers whose reviews improved the quality of this manuscript.

REFERENCES

Almuhaidib, A. M., and M. N. Toksöz, 2015, Imaging of near-surface heterogeneities by scattered elastic waves: Geophysics, **80**, no. 4, A83–A88, doi: 10.1190/geo2014-0416.1.

AlTheyab, A., F. Lin, and G. Schuster, 2016, Imaging near-surface heterogeneities by natural migration of back-scattered surface waves: Geophysical Journal International, **204**, 1332–1341, doi: 10.1093/gji/ggv511.

AlTheyab, A., E. Workman, F. Lin, and G. Schuster, 2015, Imaging near-surface heterogeneities by natural migration of back-scattered surface waves: 77th Annual International Conference and Exhibition, EAGE, Extended Abstracts, WS15-A03.

Blonk, B., G. C. Herman, and G. G. Drijkoningen, 1995, An elastodynamic inverse scattering method for removing scattered surface waves from field data: Geophysics, **60**, 1897–1905, doi: 10.1190/1.1443921.

Campman, X. H., K. van Wijk, J. A. Scales, and G. C. Herman, 2005, Imaging and suppressing near-receiver scattered surface waves: Geophysics, **70**, no. 2, V21–V29, doi: 10.1190/1.1884831.

Ernst, F. E., G. C. Herman, and A. Ditzel, 2002, Removal of scattered guided waves from seismic data: Geophysics, **67**, 1240–1248, doi: 10.1190/1.1500386.

Gottschämmer, E., and K. Olsen, 2001, Accuracy of the explicit planar free-surface boundary condition implemented in a fourth-order staggered-grid velocity-stress finite-difference scheme: Bulletin of the Seismological Society of America, **91**, 617–623, doi: 10.1785/0120000244.

Hanafy, S. M., 2015, Mapping the Qademah fault with traveltime, surface-wave, and resistivity tomograms: 85th Annual International Meeting, SEG, Expanded Abstracts, 3347–3351.

Hanafy, S. M., S. Jonsson, and Y. Klinger, 2014, Imaging normal faults in alluvial fans using geophysical techniques: Field example from the coast of Gulf of Aqaba, Saudi Arabia: 84th Annual International Meeting, SEG, Expanded Abstracts, 4670–4674.

Hyslop, C., and R. R. Stewart, 2015, Imaging lateral heterogeneity using reflected surface waves: Geophysics, **80**, no. 3, EN69–EN82, doi: 10.1190/geo2014-0066.1.

Riyanti, C. D., 2005, Modeling and inversion of scattered surface waves: Ph. D. thesis, Delft University of Technology.

Shtivelman, V., 2000, Using surface waves for mapping lateral inhomogeneities in the shallow subsurface: 6th Meeting of Environmental and Engineering Geophysics, EAGE, Extended Abstracts, SE11.

Snieder, R., 1986, 3-D linearized scattering of surface waves and a formalism for surface wave holography: Geophysical Journal International, **84**, 581–605, doi: 10.1111/j.1365-246X.1986.tb04372.x.

Stokoe, K. H., and S. Nazarian, 1985, Use of Rayleigh waves in liquefaction studies: Measurement and use of shear wave velocity for evaluating dynamic soil properties: Proceedings of a Geotechnical Engineering Division Session, American Society of Civil Engineers Convention, 1–17.

Tanimoto, T., 1990, Modelling curved surface wave paths: Membrane surface wave synthetics: Geophysical Journal International, **102**, 89–100, doi: 10.1111/j.1365-246X.1990.tb00532.x.

Virieux, J., 1986, P-SV wave propagation in heterogeneous media: Velocity-stress finite-difference method: Geophysics, **51**, 889–901, doi: 10.1190/1.1442147.

Xia, J., R. D. Miller, and C. B. Park, 1999, Estimation of near-surface shear-wave velocity by inversion of Rayleigh waves: Geophysics, **64**, 691–700, doi: 10.1190/1.1444578.

Yu, H., B. Guo, S. Hanafy, F.-C. Lin, and G. T. Schuster, 2014, Direct detection of near-surface faults by migration of back-scattered surface waves: 84th Annual International Meeting, SEG, Expanded Abstracts, 2135–2139.